Topological continuum charges of acoustic phonons in two dimensions and the Nambu-Goldstone theorem

Gunnar F. Lange [1,*] Adrien Bouhon [2,3,†] Bartomeu Monserrat [1,4,‡] and Robert-Jan Slager [1,§]

[1]*TCM Group, Cavendish Laboratory, University of Cambridge, J.J. Thomson Avenue, Cambridge CB3 0HE, United Kingdom*
[2]*Nordic Institute for Theoretical Physics (NORDITA), 114 19 Stockholm, Sweden*
[3]*Department of Physics and Astronomy, Uppsala University, Box 516, SE-751 21 Uppsala, Sweden*
[4]*Department of Materials Science and Metallurgy, University of Cambridge, 27 Charles Babbage Road,*
Cambridge CB3 0FS, United Kingdom

We analyze the band topology of acoustic phonons in 2D materials by considering the interplay between spatial/internal symmetries and additional constraints that arise from the physical context. These supplemental constraints trace back to the Nambu-Goldstone theorem and the requirements of structural stability. We show that this interplay can give rise to previously unaddressed nontrivial nodal charges that are associated with the crossing of the acoustic phonon branches at the center (Γ point) of the phononic Brillouin zone. We moreover apply our perspective to the concrete context of graphene, where we demonstrate that the phonon spectrum harbors these kinds of nontrivial nodal charges. Apart from its fundamental appeal, this analysis is physically consequential and dictates how the phonon dispersion is affected when graphene is grown on a substrate. Given the generality of our framework, we anticipate that our strategy, which thrives on combining physical context with insights from topology, should be widely applicable in characterizing systems beyond electronic band theory.

I. INTRODUCTION

The interplay between symmetry and topology has been well studied in electronic band structures for a long time, culminating in classification schemes that predict topology based only on the space group and the internal symmetries of the system [1–23]. The same machinery has also recently been applied to phononic systems [24–27], where the Bloch Hamiltonian of electrons is replaced with the dynamical matrix of phonons. The band topology of phononic systems is then described using spinless space groups, that is, the phonons are modeled using the symmetries of spinless electrons. As the dynamical matrix naturally includes time-reversal symmetry (TRS), this corresponds to the Altland-Zirnbauer (AZ) [28–30] class AI.

However, phonons are not just spinless electrons. While AZ class AI (possibly augmented by spatial symmetries) correctly captures the symmetry content of phonons, there are additional physical properties that set phonons apart from electrons. The most relevant of these [31–33] are

(1) Phonon frequencies of stable structures are nonnegative, so the dynamical matrix is positive semidefinite.

(2) Phonons (being bosons) do not couple directly to magnetic fields, so TRS is not easily broken (however, see Appendix A 2),

(3) Phonons satisfy the acoustic sum rule, e.g., they support long-wavelength excitations with vanishing frequency. These arise as a consequence of the Nambu-Goldstone (NG) theorem [34–42].

We will refer to these as additional *physical constraints*. Earlier work on phononic topology [31–33,43–59] usually incorporates these constraints by moving away from a direct dynamical matrix formulation. One strategy, introduced in Ref. [31], is to map the bosonic phonon problem to a fermionic problem [32] by considering the square root of the dynamical matrix. This replaces the positive semidefiniteness condition with a particle-hole symmetry, leading to AZ class BDI, and also gives a natural way to include TRS breaking [33,57].

Here, by contrast, we deal directly with the dynamical matrix and discuss how the additional physical constraints modify the conventional symmetry analysis. Concretely, we study the nodal charge of acoustic phonons in a 2D material at the Γ point [$q = (0, 0)$] of the Brillouin zone (BZ). Allowing the material to flex out of plane, the NG theorem [34–42,60] predicts that three acoustic bands will be degenerate at Γ, forming a triple point. We assume the presence of spinless TRS $\mathcal{T}$ throughout (discussed in Appendix A 2), e.g., $\mathcal{T}^2 = +1$ so we are in AZ class AI. As a result, the spatial symmetries of our system are described by the 80 layer groups with spinless TRS [61].

However, none of these layer groups have a three-dimensional irreducible representation (IR) [62,63], so triply degenerate points are not stabilized by internal or spatial symmetries in AZ class AI in 2D. Such triple points are therefore not anticipated from a pure symmetry analysis and arise from

*gfl25@cam.ac.uk
†adrien.bouhon@gmail.com
‡bm418@cam.ac.uk
§rjs269@cam.ac.uk

the NG theorem. Imposing such a triple point, we can then use the machinery of homotopy theory to compute the nodal charge of the triple point. This computation is simplified if the system has a unitary symmetry $\mathcal{P}$ taking $\boldsymbol{q} \to -\boldsymbol{q}$ and satisfying $(\mathcal{PT})^2 = +1$, because this allows us to restrict to real topology [2,11,64–71], as discussed in Sec. II B. We will refer to $\mathcal{P}$ as a generalized inversion symmetry. Such a symmetry does not necessarily exist globally in phononic systems, but we show in Appendix A that the physical constraints above force such a symmetry to exist close to the Γ point. In 2D, $\mathcal{P}$ is given by a twofold rotation.

We find that, with this additional symmetry, there is a nodal charge associated with the acoustic phonons in 2D. However, this charge is only associated with two of the bands, the third band being degenerate only by virtue of the NG theorem. This nodal charge assignment explains why, in 2D materials, one of the acoustic bands can gap out when the material is grown on a substrate, as confirmed experimentally for graphene [72,73]. This also follows from the NG theorem for nonrelativistic systems: The substrate allows for a violation of the NG theorem, splitting off one of the bands, whereas the other two bands are stabilized by the nodal charge. The relationship between the NG theorem and topology is discussed in Sec. V. This effect is shown explicitly in graphene in Sec. VI. Due to the generality of our approach, we emphasize that graphene is nonetheless just a specific example of this universal perspective. We note that a similar analysis was recently carried out in 3D in Ref. [74], and we comment on the connection of their results to ours throughout.

We stress the uniqueness of the retrieved 2D charges. The crossings are, as we explain, not protected by symmetry *per se*. In fact, a naive counting would suggest the absence of such crossings.

This paper is structured as follows: In Sec. II, we introduce the model for 2D acoustic phonons and discuss some general symmetry considerations. In Sec. III, we discuss the possible topology and apply it to the 2D system in Sec. IV. The relation between our topological results and the NG theorem are discussed in Sec. V. We then exemplify these concepts by applying the machinery to graphene in Sec. VI, discussing how a substrate modifies the phonon dispersion. We conclude in Sec. VII.

II. CONTINUUM MODELS FROM ELASTICITY THEORY

A. Flexural phonons in 2D

We begin by introducing a continuum model for acoustic phonons based on classical elasticity theory in 2D [75]. The

analogous model in 3D was studied in Ref. [74], and we include it for completeness in Appendix B 1 where we also discuss the model in 1D and show that it is trivial.

Classical continuum theory describes a 2D material as an elastic membrane in the xy plane which can flex in the z plane, giving rise to flexural modes [76]. The Lagrangian density for such a system is written in terms of the in-plane displacement field $\boldsymbol{u}(x, y) = (u_1(x, y), u_2(x, y))$ and the out-of plane displacement field $h(x, y)$. These fields are defined, respectively, as the in-plane and out-of-plane deviations of the atoms from their equilibrium position. Explicitly, the Lagrangian density for a flexible membrane is given by [75,77,78]

$$\mathcal{L} = \frac{\rho_0}{2}(\dot{\boldsymbol{u}}^2 + \dot{h}^2) - \frac{1}{2}\kappa_0(\nabla^2 h)^2 - \mu \overleftrightarrow{u}_{ij}^2 - \frac{1}{2}\lambda \overleftrightarrow{u}_{kk}^2, \quad (1)$$

where μ and λ are Lamé parameters and ρ_0 and κ_0 are the stiffness in and out of plane, respectively. The strain tensor $\overleftrightarrow{u}_{ij}$ is defined as

$$\overleftrightarrow{u}_{ij} = \frac{1}{2}(\partial_i u_j + \partial_j u_i + \partial_i h \partial_j h). \quad (2)$$

Expanding Eq. (1) to quadratic order in the displacements defines what we will refer to as the *harmonic approximation*. This is valid whenever phonon-phonon interactions are negligible, which we assume throughout (for a discussion of such terms, see Ref. [78]). Note that we do not restrict our model to be quadratic in the wave vectors $\boldsymbol{q}$. Looking for plane-wave solutions to the equations of motion gives the classical wave equation with general form

$$D(\boldsymbol{q})\boldsymbol{v}(\boldsymbol{q}) = \omega^2(\boldsymbol{q})\boldsymbol{v}(\boldsymbol{q}), \quad (3)$$

where $\boldsymbol{q} = (q_x, q_y)$ is the wave vector of the plane wave, $D(\boldsymbol{q})$ is the dynamical matrix, whose topology we investigate, $\omega^2(\boldsymbol{q})$ are the eigenfrequencies, and $\boldsymbol{v}(\boldsymbol{q}) = (\boldsymbol{u}, h)$. Note that a continuum model can never capture optical branches in the phonon spectrum, as they depend on the internal motion of atoms which we neglect. As we are only interested in the topology of the acoustic phonons close to Γ [e.g., $\boldsymbol{q} = (0, 0)$], the optical branches will have no impact on our analysis. A more realistic model describing the phonons of graphene is analyzed in Sec. VI. For now, we think of $D(\boldsymbol{q})$ as a $\boldsymbol{k} \cdot \boldsymbol{p}$ expansion of the full (many-band) phonon band structure around Γ, describing the lowest three bands.

For stable structures, $D(\boldsymbol{q})$ is positive semidefinite, so ω is real. A more careful analysis of the constraints on $D(\boldsymbol{q})$ is performed in Appendix A. For the Lagrangian in Eq. (1), we find

$$D(\boldsymbol{q}) = \begin{pmatrix} v_l^2 q_x^2 + v_t^2 q_y^2 & (v_l^2 - v_t^2)q_x q_y & 0 \\ (v_l^2 - v_t^2)q_x q_y & v_l^2 q_y^2 + v_t^2 q_x^2 & 0 \\ 0 & 0 & v_h^2(q_x^4 + 2q_x^2 q_y^2 + q_y^4) \end{pmatrix}. \quad (4)$$

Solving the eigenvalue problem in Eq. (3) gives explicitly

$$\omega_1^2 = v_h^2 \boldsymbol{q}^4, \quad \omega_2^2 = v_t^2 \boldsymbol{q}^2, \quad \omega_3^2 = v_l^2 \boldsymbol{q}^2. \quad (5)$$

The associated eigenvectors then read

$$\boldsymbol{v}_1 = \begin{pmatrix} 0 \\ 0 \\ 1 \end{pmatrix}, \quad \boldsymbol{v}_2 = \frac{1}{|\boldsymbol{q}|} \begin{pmatrix} -q_y \\ q_x \\ 0, \end{pmatrix}, \quad \boldsymbol{v}_3 = \frac{1}{|\boldsymbol{q}|} \begin{pmatrix} q_x \\ q_y \\ 0 \end{pmatrix}, \quad (6)$$

where $v_l = \sqrt{(2\mu + \lambda)/\rho_0}$, $v_t = \sqrt{\mu/\rho_0}$, and $v_h = \sqrt{\kappa_0/\rho_0}$ are the longitudinal, transverse and out-of plane velocities, respectively. We therefore get a triple degeneracy at $\boldsymbol{q} = (0, 0)$ with $\omega = 0$, and with two linear bands and one quadratic band crossing as shown in Fig. 1. The quadratic band corresponds to the out-of plane flexural mode and it is well-known [76,79,80] that such bands are generically present in 2D materials. This quadratic band distinguishes the 2D case from the 3D case studied in Ref. [74]. We note that the flexural band is completely decoupled from the in-plane modes. This is not just a feature of our simplified model: the bands remain decoupled as long as the harmonic approximation remains valid (e.g., we can ignore phonon-phonon couplings). The more realistic model for graphene considered in Sec. VI exhibits the same decoupling. In graphene, this can also be understood as arising from the fact that the flexural and in-plane bands have opposite eigenvalues under the horizontal mirror operation [24]. We will argue below that this decoupling, a feature of the 2D case, is intimately tied to the nodal charge of the triple point.

We finally note that the bands $\boldsymbol{v}_2$ and $\boldsymbol{v}_3$, respectively, correspond to a divergence-free angular vector field and a curl-free radial vector field, as illustrated in Figs. 1(c) and 1(d). This simplifies computation but is not a generic feature of flexural phonons.
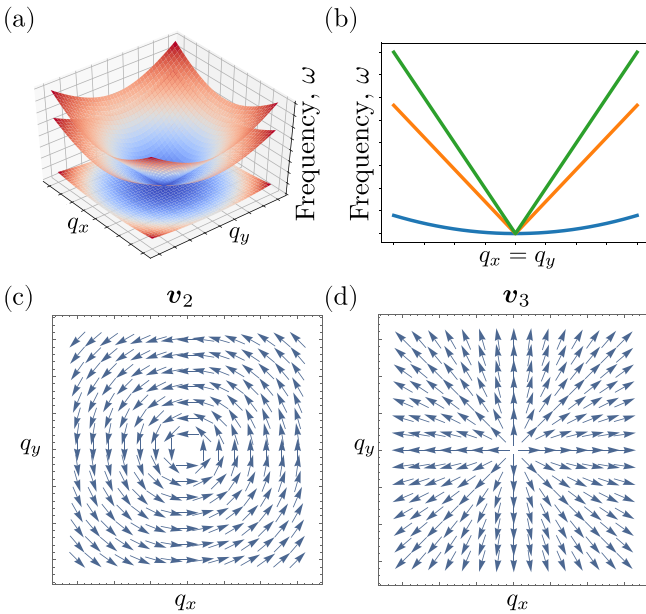

FIG. 1. Summary of the dynamical matrix specified in Eq. (4). (a) Band structure in 3D with $v_t = v_h = 1$ and $v_l = 2$, (b) same as (a) but along the line $q_x = q_y$, where the lowest band (blue) is the flexural band, (c) vector field corresponding to the eigenvector $\boldsymbol{v}_2 = |\boldsymbol{q}|^{-1}(-q_y, q_x, 0)$, see Eq. (4), (d) vector field corresponding to the eigenvector $\boldsymbol{v}_3 = |\boldsymbol{q}|^{-1}(q_x, q_y, 0)$.

B. Symmetry considerations in 2D

As mentioned in the Introduction, we assume throughout that our models are nonmagnetic (have spinless time-reversal symmetry $\mathcal{T}$) and have a generalized inversion symmetry $\mathcal{P}$, which satisfy $(\mathcal{PT})^2 = +1$. The physical constraints make these assumptions valid close to Γ quite generally, as discussed in Appendix A. We represent the antiunitary symmetry $\mathcal{T}$ as $\mathcal{T} = \mathcal{U}\mathcal{K}$, where $\mathcal{U}$ is the (unitary) orbital action and $\mathcal{K}$ is complex conjugation. Acting with $\mathcal{P}$ and $\mathcal{T}$ on $D(\boldsymbol{q})$ gives that $D(\boldsymbol{q})$ must satisfy

$$\mathcal{U}D^*(-\boldsymbol{q})\mathcal{U}^{-1} = D(\boldsymbol{q}), \quad \mathcal{P}D(-\boldsymbol{q})\mathcal{P}^{-1} = D(\boldsymbol{q}). \quad (7)$$

This, together with the assumption that $(\mathcal{PT})^2 = +1$, implies that there exists a basis in which $\mathcal{PT} = \mathcal{K}$, so $D(\boldsymbol{q})$ can be chosen to be a real symmetric matrix [65]. In the language of Ref. [68], we are in AZ+$\mathcal{I}$ class AI. For the model in Eq. (4), $\mathcal{U} = \mathcal{P} = \mathbb{1}$.

In addition to this symmetry class, however, we are also impacted by the NG theorem [34,35], which in essence states that whenever a continuous symmetry is spontaneously broken, massless bosons must appear. Generically, one expects the number of Goldstone bosons to be equal to the number of broken symmetries. By imposing a lattice, we are breaking both continuous translational and rotational symmetries. However, these symmetries are linked [36–42] so that we only get three massless bosons, as discussed further in Sec. V.

As remarked in the Introduction, there are no 3D irreducible representations (IRs) in the 2D layer groups in AZ class AI. Therefore, the triple point at Γ must consist of at least two IRs, which are glued together by the NG theorem. This gluing of IRs is not protected by symmetry in 2D. This can also be seen from a codimension argument [68]: $\mathcal{PT}$ symmetry forces $D(\boldsymbol{q})$ to be an element of SO(3), which is generated by the three rotation matrices $L_{i=x,y,z}$, The triple band touching then requires tuning three independent parameters, but there are only two momentum components available to tune. Therefore, this triple crossing cannot be stable, in general, and only arises due to the NG theorem. We confirm this in Secs. V and VI by showing that when the NG theorem is modified by adding a substrate, the triple degeneracy is lifted to a double degeneracy. This agrees with our analysis in Sec. IV, where we show that this double degeneracy has an associated nontrivial nodal charge. This illustrates that the NG theorem can impose constraints on the band structure beyond any symmetry formulation.

III. TOPOLOGICAL ANALYSIS FROM A HOMOTOPY PERSPECTIVE

In this section, we investigate the topology associated with the nodal point between the acoustic bands at $\boldsymbol{q} = \boldsymbol{0}$. Topological charges of nodal points can generally be diagnosed by considering the homotopy group of the classifying space [81].

To find the classifying space of our model, we note that the first Lamé parameter in Eq. (1) satisfies $\mu > 0$ [75]. The second Lamé parameter λ can be negative, but is positive for most materials [82,83]. We therefore generically expect $v_l > v_t$. As we are working with an elastic continuum model,

TABLE I. Possible charge of triple point for acoustic phonons of various dimensions. $\mathbb{Q}$ denotes the quaternion group. The $\mathbb{Z}_2$ charge corresponds to the first Stiefel-Whitney class on a loop around the nodal point [87] and the $2\mathbb{Z}$ charge corresponds to the Euler class on a sphere surrounding the nodal point (discussed in Ref. [74]).

Name	M	$\pi_0(M)$	$\pi_1(M)$	$\pi_2(M)$
$Fl^{\mathbb{R}}_{1,1,1}$	$SO(3)/D_2$	$\mathbb{0}$	$\mathbb{Q}$	$\mathbb{0}$
$Gr^{\mathbb{R}}_{2,3}$	$\mathbb{R}P^2$	$\mathbb{0}$	$\mathbb{Z}_2$	$2\mathbb{Z}$

our model is only valid when the wavelengths we are considering are much larger than the interatomic spacing, which corresponds to small $\boldsymbol{q}$. In this limit, we expect $\omega_1 < \omega_2 < \omega_3$ away from $\boldsymbol{q} = \boldsymbol{0}$, so we are considering three separate phonon branches (a $1 \oplus 1 \oplus 1$ split). This should be contrasted with the continuum model in 3D (see Ref. [74] and Appendix B 1), where there are three linear bands, two of which are degenerate (a $2 \oplus 1$ split). In 2D, additional symmetries may force the two linear bands to become degenerate along high-symmetry lines, resulting in a $2 \oplus 1$ split.

Because of our assumed $\mathcal{PT}$ symmetry, we can always choose $D(\boldsymbol{q})$ to be a real symmetric matrix (see Sec. II B and Appendix A), such that its eigenvectors ($\boldsymbol{v}_1, \boldsymbol{v}_2, \boldsymbol{v}_3$) are real and their collection, i.e., the frame of eigenvectors, forms an element of O(3). Under the reality condition, each eigenvector has a ± 1 sign as a gauge freedom. We can thus always locally choose a gauge where the frame has positive determinant, i.e., it is an element of SO(3). Dividing out by the group of gauge transformations that preserve the energy ordering of the bands, as well as the handedness of the frame, we obtain the classifying space $Fl^{\mathbb{R}}_{1,1,1} = SO(3)/S[O(1) \times O(1) \times O(1)]$ for the $1 \oplus 1 \oplus 1$ split [11]. This is the (unoriented) real complete Flag variety. It is also convenient to consider the group of gauge transformations as the sign-exchange of each pair of eigenvectors, i.e., the group of π rotations along each of the three eigenvectors. This corresponds to the point group $D_2 = \{E, C_{2,\boldsymbol{v}_1}, C_{2,\boldsymbol{v}_2}, C_{2,\boldsymbol{v}_3}\}$, and the classifying space then takes the compact form $Fl^{\mathbb{R}}_{1,1,1} = SO(3)/D_2$ [70]. For the $2 \oplus 1$ split, the classifying space reduces to the real (unoriented) Grassmannian $Gr^{\mathbb{R}}_{2,3} = SO(3)/S[O(2) \times O(1)]$, which is isomorphic to the real projective plane, i.e., $Gr^{\mathbb{R}}_{2,3} \simeq \mathbb{R}P^2$.

The topological charge of a nodal point in D dimensions for a system with classifying space M is generically captured by the homotopy group $\pi_{D-1}(M)$ [68]. These groups can be computed using long exact sequences, as described in Ref. [84]. The results given in Refs. [68,70] are summarized in Table I. As we are only interested in the local topology of the node, we only need to consider base loops and base spheres, such that the homotopy groups are sufficient to classify the topological nodal phases. Indeed, global topologies, i.e., over the whole BZ $\mathbb{T}^D$, requires the consideration of homotopy equivalence classes $[\mathbb{T}^D, M]$ which can have more structure, such as nontrivial lower dimensional topologies over the noncontractible cycles of the BZ torus, as e.g., the first Stiefel-Whitney class [85], computed along a full lattice vector, and the action of the generators of $\pi_1[M]$ on the second homotopy group [11,67,86]. It follows that the question of orientability for $d > 1$-dimensional topologies is not relevant

for us since the continuous maps $\mathbb{S}^{d>1} \to M$ always induce an orientation, e.g., any mapping $\mathbb{S}^2 \to \mathbb{R}P^2$ can be decomposed into a winding component $\mathbb{S}^2 \to \mathbb{S}^2$ and an orientable double cover $\mathbb{S}^2 \to \mathbb{R}P^2$ [11].

We note that some entries in Table I capture fragile topology, in the sense that adding additional trivial bands can change their value. The $\mathbb{Z}_2$ charge (corresponding to the first Stiefel-Whitney class [85,87]) is stable under the addition of trivial bands. The quaternion charge $\mathbb{Q}$ turns into the Nth Salingaros group under addition of further bands [65,70]. Finally, the $2\mathbb{Z}$ charge (corresponding to the Euler class [11,65,85,88], see below) turns into a $\mathbb{Z}_2$ charge, the second Stiefel-Whitney class, under the addition of additional bands [85,87]. As we are only concerned with the acoustic bands, this low-band limit is justified.

We finally note that the 3D topology of a nodal point, characterized by the topology over a sphere wrapping the node, was considered in Ref. [74] for the $2 \oplus 1$ split, in which case it was classified by the Euler class. Note that, as discussed there, the presence of this split requires that the condition $v_l > v_t$ be satisfied along the high-symmetry lines emanating from Γ. Otherwise, the three bands cannot be split on any sphere surrounding Γ, so there is no nodal charge (since then SO(3) gauge transformations are allowed, thus trivializing the classifying space $SO(3)/SO(3) = 1$ [89]). In contrast, for 2D phonons, the topology is always well-defined. Sufficiently close to Γ, the flexural mode will always be at lower frequency than the in-plane modes, owing to the quadratic dispersion. Thus, violating the condition that $v_l > v_t$ along high-symmetry lines can only change the split from $1 \oplus 1 \oplus 1$ to $2 \oplus 1$ in 2D. As can be seen in Table I, this results in a reduction of the nodal charge from $\mathbb{Q}$ to $\mathbb{Z}_2$, but it does not *a priori* completely remove the topology (however, see Sec. IV B for a caveat to this). Therefore, the nodal charge in 2D is actually more stable than its 3D counterpart as can be defined in all 2D systems with $\mathcal{PT}$ symmetry. In 1D, discussed briefly in Appendix B 2, the situation is slightly different as there is a fourth, torsional, acoustic mode. However, the $\pi_0(M)$ charge of the relevant classifying spaces M, listed in Appendix B 2, is still trivial, so there is no topological nodal charge in 1D.

IV. TOPOLOGY OF 2D ACOUSTIC PHONONS

We now consider the topology of the 2D case in further detail. In 2D, the only possible homotopy classifications are $\pi_p(X)$ for $p \in \{0, 1, 2\}$ [68]. π_2 charges correspond to considering monopoles encapsulated by a surface, e.g., the BZ or patches thereof. These are therefore irrelevant to the nodal charges in 2D as they are classified by loops around nodes. Furthermore, as can be seen in Table I, the π_0 charge is zero in all symmetry settings. Thus, the only relevant invariant is the π_1 charge, which corresponds to taking a circle around the triple point at Γ. Depending on whether the bands split as $2 \oplus 1$ or $1 \oplus 1 \oplus 1$ over this circle, the relevant groups are either $\mathbb{Z}_2$ or the quaternion group $\mathbb{Q}$ (see Table I). We investigate both charges in this section. We assume throughout that the three acoustic bands are separated in energy from all other bands on a circle around the triple point at Γ, and on the entire disk enclosed by this circle.

A. Quaternion charge of the complete Flag variety

When the bands split as $1 \oplus 1 \oplus 1$, the relevant π_1 charge is the quaternion group $\mathbb{Q}$. We are therefore *a priori* dealing with non-Abelian nodal charges. Non-Abelian charges in band structures is a novel but quickly growing field [11,65–68,70,71,90,91,93,94]. For the quaternion group, there are five conjugacy classes of stable nodal charges: $\{1, -1, \pm i, \pm j, \pm k\}$, which correspond to combinations of nodes in various gaps [67,90]. Here i, j, k satisfy $i^2 = j^2 = k^2 = ijk = -1$. In general, the charges i, j, k are only defined up to equivalence because their sign is gauge dependent [90], as discussed further in Sec. IV A 2.

We discuss below two approaches to compute the topological charge of the crossing at Γ. We first determine the frame-rotation phase on a loop encircling the node. We then split the threefold degeneracy into two-band nodes and compute their Euler class [65,88,90]. Such a splitting is physically relevant for 2D systems on a substrate, as we discuss in Sec. VI. We find that both charges agree with the quaternion charge -1. Finally, we also relate to the more familiar notion of Berry phase in Sec. IV A 3 and show that it is insufficient to capture the topology.

1. Frame rotation charge

We here compute the frame rotation charge of the node, i.e., the geometric angle of the rotation of the parallel-transported frame on the base loop around the node. The frame rotation charge measures the ability of a pair of nodes to annihilate inside the disk bounded by the base loop. It derives from $\pi_1[SO(N)] = \mathbb{Z}_2$ for $N \geqslant 3$. For the specific case of $N = 3$, consider a matrix of three ordered orthonormal vectors (usually called a frame) $F = (\boldsymbol{v}_1, \boldsymbol{v}_2, \boldsymbol{v}_3)$. In our case, these vectors correspond to the eigenstates of the acoustic bands. Thanks to the analytical expression of the eigenvectors in Eq. (6), we know an unambiguous global gauge and the frame rotation charge can be readily obtained as in Ref. [95]. Moving along a closed trajectory Δ in the BZ, we induce a mapping $R(\boldsymbol{q}) = F(\boldsymbol{q})^T F(\boldsymbol{q}_0)$, with $\boldsymbol{q}_0$ a fixed reference point, and $\boldsymbol{q}$ traversing Δ. By deforming Δ to a loop parametrized by an angle $\theta \in [0, 2\pi]$, this becomes a map from S^1 to the space of frames. This mapping can be decomposed into the basis elements $\{L_i\}_{i=x,y,z}$ of the Lie algebra SO(3), as $R(\theta) = \exp[\sum_{i=x,y,z} \varphi_i(\theta) L_i]$. The accumulated frame rotation charge is then

$$\varphi(\theta) = \sqrt{\sum_{i=x,y,z} \varphi_i(\theta)^2}. \qquad (8)$$

If we require the frames to be completely equivalent after traversing Δ, then the entire trajectory $R(\theta)$ lies in SO(3) and $\varphi(2\pi) = 2\pi n$ for $n \in \mathbb{Z}$. By using the connection to the spin group, one can show [65,95] that φ is periodic modulo 4π, in analogy to the Dirac belt trick. This agrees with $\pi_1[SO(3)] = \mathbb{Z}_2$ and shows that there are two possible charges $\varphi(2\pi) = \{0, 2\pi\} \bmod 4\pi$. If, however, we allow the final frame to differ from the initial frame by a sign change of two eigenvectors (as allowed by the gauge degree of freedom), then the frame modulo the gauge transformation describes a closed loop in $SO(3)/D_2$, and $\varphi(2\pi) = \pi \bmod 4\pi$ becomes a

possible solution [$\varphi(2\pi) = 3\pi$ only differs from $\varphi(2\pi) = \pi$ by a gauge transformation].

To discuss the physical interpretations of φ, we introduce some standard terminology for three-band systems [65,70]. We refer to the gap between the lowest-energy band and the middle band as the *principal gap*, and a node in this gap is therefore a *principal node*. Similarly, the gap between the middle band and the highest-energy band is referred to as the *adjacent gap*, and nodes in this gap are *adjacent nodes*. Note that these concepts are ill-defined for the triple degeneracy but become well-defined once we imagine infinitesimally, splitting the triple degeneracy as discussed in Sec. IV A 2. If there are no stable nodes between the eigenstates that constitute $F(\boldsymbol{q})$ on or inside the trajectory Δ, then the frame is smooth everywhere and $\varphi(2\pi) = 0 \bmod 4\pi$. This corresponds to the trivial quaternion charge $+1$. If there is a stable double node in either the principal or the adjacent gap, then the frame must perform a 2π rotation around the node, so $\varphi(2\pi) = 2\pi \bmod 4\pi$ corresponds to quaternion charge -1. Finally, if there is a simple node in the principal gap, or the adjacent gap, or in both gaps, the frame performs a π rotation so $\varphi(2\pi) = \pi \bmod 4\pi$ corresponds to quaternion charges i, j, k [by resolving $R(\theta)$ in the three angular momentum matrices, we can determine the corresponding quaternion charge]. Thus, the frame rotation charge captures the stability of a pair of nodes or of single nodes. This is addressed further in Sec. IV A 2 and Appendix C.

Concretely, for the continuum model in Eq. (4), the mapping R, formed by the eigenstates of the model with fixed base point $\boldsymbol{q}_0 = (r, 0)$, for some $r > 0$, is given by

$$R(\boldsymbol{q}) = F^T(\boldsymbol{q}) F(\boldsymbol{q}_0) = \frac{1}{|\boldsymbol{q}|} \begin{pmatrix} |\boldsymbol{q}| & 0 & 0 \\ 0 & q_x & q_y \\ 0 & -q_y & q_x \end{pmatrix}, \qquad (9)$$

where we have ordered the eigenstates by frequency ω and we have chosen a smooth gauge. Parameterizing R by planar polar coordinates (r, θ) then gives

$$R(\theta) = e^{\theta L_x}. \qquad (10)$$

Note that this corresponds to a rotation around a fixed axis. This is something we expect to hold more generally, due to the decoupling of the flexural mode from the in-plane modes, discussed in Sec. II A. When traversing the entire loop, Eq. (10) gives $\varphi(2\pi) = 2\pi \bmod 4\pi$, which gives a quaternion charge of -1, indicating that there is a stable pair of nodes forming a double node at Γ in the continuum model.

We briefly discuss the computation of the quaternion charges when a global analytical expression of the eigenvectors is not known, i.e., when they must be computed numerically. In that case, one starts with the discretization of the base loop, one regularizes the gauge signs of the eigenvectors, and one lifts the projections $R(\boldsymbol{q}_i) = F(\boldsymbol{q}_i)^T \cdot F(\boldsymbol{q}_{i-1})$ to the double spin cover SU(2) [70,91,92], see also Appendix C. The lift to the spin group permits the use of the log function to obtain the accumulated phase components in the Lie algebra (indeed, the radius of convergence for the log function is doubled from SO(3) to SU(2)). One can alternatively compute the Lie algebra components in SO(3) directly, by using the

log of the Baker-Campbell-Hausdorff formula, as given in Ref. [70].

2. Quaternionic charge and Euler class

While the frame rotation charge suffices to determine whether or not there is a protected nodal charge associated with the bands, it does not distinguish nodes in different gaps. This is significant, as the flexural mode at Γ can be gapped away from zero frequency under certain conditions [72,73]. This happens for graphene grown on certain substrates, and the magnitude of this splitting is sometimes used as a rough indicator of the interaction between the substrate and the graphene layers [73,96,97]. The substrate modifies the out-of-plane symmetry breaking, so the NG theorem cannot be straightforwardly applied, as discussed in Sec. V, and therefore the triple degeneracy is not required. Note that if the interaction with the substrate is sufficiently weak and the acoustic bands remain separated from all other bands, then the nodal charge of free-standing graphene should still be applicable to the case of graphene on a substrate. We show in Sec. VI that this nodal charge is nontrivial, suggesting that the nodal charge only protects the crossing of the in-plane bands. To investigate this further, we now discuss how to distinguish the charge of nodes in different gaps using the Euler class [65,81,84,88].

The Euler class is defined for two-band subspaces of three-band *real* Hamiltonians, in analogy to the more familiar Chern class for complex Hamiltonians. The Chern class is an integer obtained by integrating the Berry curvature (a differential two-form) over closed, even dimensional manifolds. Similarly, the Euler class between states $|v_1(\mathbf{q})\rangle$ and $|v_2(\mathbf{q})\rangle$ is an even integer obtained by integrating the Euler form,

$$\mathrm{Eu}(\boldsymbol{q}) = \langle \boldsymbol{\nabla} v_1(\boldsymbol{q})| \times |\boldsymbol{\nabla} v_2(\boldsymbol{q})\rangle, \qquad (11)$$

over closed even dimensional manifolds. In fact, the Euler form can be understood as the Berry curvature of the state $|v_1(\boldsymbol{q})\rangle + i|v_2(\boldsymbol{q})\rangle$ [65]. The Euler class is only defined for orientable vector bundles, i.e., for band subspaces with trivial first Stiefel Whitney class (equivalently, with zero Berry phase), but this is not a problem for the continuum model as there are no noncontractible loops in the plane.

Note that the only closed, even-dimensional manifold available in 2D is the whole BZ, which makes it difficult to compute these quantities in a continuum model (where the BZ corresponds to all of $\mathbb{R}^2$). However, for the Euler class, a patch formulation exists (e.g., it is possible to compute it on a subset of $\mathbb{R}^2$) as discussed in Refs. [65,66,88,90–92]. The *patch Euler class* over a patch $\mathcal{D}$ is defined as

$$\chi(\mathcal{D}) = \frac{1}{2\pi}\left[\int_{\mathcal{D}} \mathrm{Eu} - \oint_{\partial\mathcal{D}} a \right] \in \mathbb{Z}, \qquad (12)$$

where $\partial\mathcal{D}$ is the boundary of $\mathcal{D}$. Furthermore, Eu is the Euler two-form in Eq. (11) which can alternatively be defined as $\mathrm{Eu} = d\mathrm{a} = d\mathrm{Pf}\mathcal{A}$, where $\mathcal{A}_{ij} = \langle v_i(\boldsymbol{q})|dv_j(\boldsymbol{q})\rangle = \boldsymbol{A}_{ij} \cdot d\boldsymbol{q} = \sum_{\alpha=x,y}\langle v_i(\boldsymbol{q})|\partial_{q_\alpha} v_j(\boldsymbol{q})\rangle dq_\alpha$ in terms of the band indices $i, j \in \{1, 2\}$. The second term in Eq. (12) then amounts to the integral of the Euler connection one-form a $= \mathrm{Pf}\boldsymbol{A} \cdot d\boldsymbol{q}$. We note that this definition intimately profits from the reality conditions of the two-band Berry connections ensuring that it

takes values in the orthogonal Lie algebra SO(2). The integer $\chi(\mathcal{D})$ equals half the number of stable nodes between the two bands inside $\mathcal{D}$ [88]. This should be contrasted with the Chern class, where no patch formulation is readily obtainable without gauge fixing, showing that the Euler class is an ideal tool for analyzing continuum models.

One characteristic feature of Euler class topology is that there can be multiple nodes in the same gap that are unable to annihilate. To correctly capture this property, a consistent gauge assignment must be made. This is done by drawing Dirac strings between any pair of nodes, which correspond to branch cuts across which the gauge must change. Detailed rules for assigning such strings can be found in Refs. [90–92]. Most importantly, whenever a principal node (see previous section) crosses the Dirac string of an adjacent node, or vice versa, its chirality must flip. This leads to nontrivial braiding statistics and non-Abelian charges. Knowing which gap hosts stable nodes, one can then assign quaternion charge i for single nodes in the principal gap, j for nodes in the adjacent gap, k for one node in both gaps, and -1 for a double node in either gap [70]. Note that the signs of i, j, k flip when crossing a Dirac string [88], which explains the assertion made above that the i, j, k are only defined modulo a sign. The charge -1 corresponds to a double node and is therefore unaffected by crossing a Dirac string, giving rise to the aforementioned five equivalence classes.

The patch Euler class is only well-defined for two-band subspaces, so the patch must be chosen so as to only contain either principal or adjacent nodes. This is clearly not possible for the triple point. This can be circumvented by artificially adding a term to our dynamical matrix which splits the triple degeneracy into principal and adjacent nodes. If this splitting can be adiabatically mapped back to the original triple point, then the charge of the principal/adjacent nodes should reflect the charge of the triple point.

To make this concrete, we consider the continuum model of Eq. (4). If we wanted to capture the physics of graphene on a substrate discussed in Refs. [72,73] and Sec. VI, we should lift the flexural band up in frequency. However, this leads to nodal lines rather than nodal points. We perform this lifting for graphene in Sec. VI. Here, we instead add an onsite energy to one of the orbitals contributing to the linearly dispersing bands, modifying $D(\boldsymbol{q})$ from Eq. (4) as

$$\tilde{D}(\boldsymbol{q}) = D(\boldsymbol{q}) + \mathrm{diag}\{\epsilon, 0, 0\}. \qquad (13)$$

Note that because $v_l \neq v_t$ in our model, this will break C_4 invariance, but maintain C_2T invariance (as well as C_2 and T separately), and therefore the reality condition. This splits the triple point into two adjacent nodes on the q_y axis and a single principal node at Γ. This is illustrated in Fig. 2(b). Computing the Euler class over an annulus/disk avoiding the principal/adjacent node, using the code in Ref. [98], we find that the principal node at the center has $\chi = 0$, corresponding to quaternion charge $+1$. The adjacent nodes on the q_y-axis have a combined Euler class of $\chi = -1$, giving a corresponding quaternion charge of -1. Combining the nodes by taking $\epsilon \to 0$ gives that the total quaternionic charge is -1, in agreement with what was found using the frame rotation charge in the previous section. However, knowing the gap structure, we now know that this charge is associated only with the
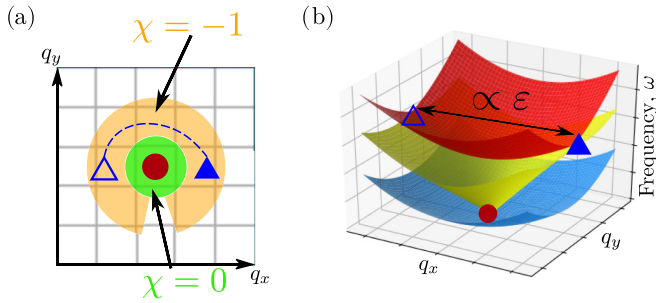
FIG. 2. (a) Schematic of the Euler class computation, following the graphical notation from Ref. [90]. Perturbing the dynamical matrix in Eq. (4) by an on-site term of magnitude ϵ creates two nodes in the adjacent gap (blue triangles) with opposite chirality (empty/filled) connected by a Dirac string and one principal node in the center (red cirlce) with trivial charge. This is confirmed by computing the patch Euler class over the orange annulus ($\chi = -1$) and over the green circle ($\chi = 0$). (b) The band structure corresponding to the situation sketched in (a). The code used is available at Ref. [98].

crossing between the linear bands [99]. Thus, the crossing between the quadratic and the linear bands is not topologically protected, whereas the crossing between the linear bands is protected. Note that because the nodal charge represents the generator of $\pi_1[SO(3)] = \mathbb{Z}_2$, and that $\pi_1[SO(N)] = \mathbb{Z}_2$ for all $N \geqslant 3$, this charge is actually stable in the many-band limit. We emphasize that this node cannot be obtained from an irreducible representation (IR analysis), as it is present even in layer groups without 2D IRs.

This result can be understood straightforwardly by noting that adding any perturbation of the form diag$\{0, \delta, 0\}$ to $\tilde{D}(\boldsymbol{q})$ (with $\delta > 0$, e.g., adding another on-site term) will completely remove the principal node. This is therefore an accidental node, in the sense that it is not symmetry protected. It is, however, protected by the NG theorem as it cannot be removed without modifying the conditions of the theorem (i.e., by adding a substrate). This also implies that there are strong constraints preventing the lifting of the in-plane acoustic modes, e.g., if the NG theorem is broken adiabatically, we only expect the flexural band to gap out (though the crossing point between the linear bands may shift in frequency).

We now argue why we *generically* expect nodal charges of $\{+1, -1\}$ for acoustic phonons in systems that have $\mathcal{P}$ and $\mathcal{T}$ symmetry separately (rather than just their product). As discussed in Sec. II B and elaborated on in Appendix A, this is in fact a very general condition when sufficiently close to Γ, as a consequence of the physical constraints on the phonons.

Time-reversal symmetry $\mathcal{T}$ implies that if there is a band touching at $\boldsymbol{q}$, then there will also be a band touching, between the same bands, at $-\boldsymbol{q}$. Let us assume without loss of generality that the node at $\boldsymbol{q}$ has charge $+i$. Then the node at $-\boldsymbol{q}$ has charge $\pm i$ (the sign depends on the location of the Dirac strings from the adjacent nodes). Now imagine splitting the triple point into two pairs of nodes in each gap (as required by the presence of $\mathcal{T}$). Let us assign charge $\pm i$ to nodes in the first gap and $\pm j$ to nodes in the second gap. The total node configuration at the triple point will then have charge $Q =$

$(\pm i)(\pm i)(\pm j)(\pm j)$, where the order of the factors depends on the details of how the nodes are adiabatically brought together. Regardless of the order, however, the only possible result is $Q = \pm 1$. Thus, generically (that is, unless there is a symmetry beyond the NG theorem pinning the nodes at Γ), we expect the quaternionic charge to reduce to ± 1. Thus, the physical constraints can give topology beyond what is expected from symmetry analysis but they also constrain the nodal charge beyond the symmetry analysis.

3. Relating to Berry phase

We now relate the above findings to the more conventional Berry phase formulation of nodal charges and show that Berry phases are insufficient to capture this topology.

For a single band in a system with generalized $\mathcal{PT}$ symmetry, the only gauge freedom is a choice of sign. If the sign of the eigenvector necessarily flips as it is transported around the loop, there must be a discontinuity in the gauge somewhere along the loop due to the discreteness of the gauge group (this corresponds to the Dirac string discussed above). This indicates that the band under consideration forms an odd number of topologically protected nodes within the loop. As discussed in Refs. [85,87], such a discontinuity can be analyzed by using a smooth *complex* gauge, where a Berry phase of π indicates a sign reversal. Thus, along the loop, each band can (in a smooth complex gauge) have a Berry phase of 0 or π.

As we assume the acoustic bands to be separated from all other bands on the loop and the disk it encloses, the sum of the Berry phases of the three acoustic bands must be 0 mod 2π (because a single node induces a Berry phase of π in *both* bands forming the node). We write the Berry phases of the bands as $\vec{\varphi} = (\varphi_1, \varphi_2, \varphi_3)$, where we have ordered the bands by frequency ω on the loop. Thus, e.g., the phases $(\pi, \pi, 0)$ indicate a principal node, $(0, \pi, \pi)$ indicate an adjacent node, and $(\pi, 0, \pi)$ indicate one principal and one adjacent node. These, respectively, correspond to quaternion charge i, j, k. Note that the Berry phase $(0,0,0)$ can correspond to quaternion charge $+1$ or -1, as the Berry phase is oblivious to the presence of double nodes.

In the specific case of flexural phonons, we expect the lowest energy flexural band to be accidentally coupled to the other two bands, as discussed in Sec. IV A 2, so it necessarily has a trivial Berry phase. Therefore, the only possible assignments of Berry phase are $\vec{\varphi} = \{(0, 0, 0), (0, \pi, \pi)\}$. From the above discussion, we generically expect a quaternion charge of ± 1 in systems with TRS, leaving only $\vec{\varphi} = (0, 0, 0)$. Thus, the nodal charge of acoustic phonons in 2D is completely invisible to the Berry phase.

B. $\mathbb{Z}_2$ charge of the real Grassmannian in 2D

The above discussion applies when all three bands can be split on a loop around Γ. If there is a symmetry which forces the two linear bands to be degenerate, either along high-symmetry lines or everywhere, then any loop around the triple point will necessarily contain a node between the linear bands. Thus, the classifying space is the real Grassmannian and the associated π_1 charge in Table I is $\mathbb{Z}_2$, which corresponds to the first Stiefel-Whitney class as discussed in Ref. [87]. This invariant measures the orientability of the real wave function as

one traverses a loop. Specifically, this corresponds to whether or not there is (necessarily) a sign reversal of the subframe spanned by the bands under consideration. This number can be defined for either the flexural mode or the two linearly dispersing modes. For the flexural mode, it corresponds to the Berry phase computed in a smooth complex gauge as also discussed in Sec. IV A 3. Because there is no coupling between the flexural and the linearly dispersing bands in the harmonic approximation, the flexural mode is trivial and therefore there exists an obvious gauge in which the orientation is constant. Thus, the first Stiefel-Whitney invariant is trivial for the flexural band.

To conclude, we rely on a global cancellation condition: the Berry phase of all three bands must be zero, since these bands are disconnected from all other bands at higher frequency ω (indeed, a resultant π-Berry phase indicates an unavoidable node with the other bands). This is to be contrasted with the quaternion charges of the frame, since the nontrivial frame charges indicate stable nodes among the three bands of the frame and not with the other bands. We furthermore note that a nontrivial quaternion charge of -1 (Euler class of ± 1) around a region of the BZ is not required to be canceled by compensating nodes in any other region of the BZ, contrary to the Berry phase and the quaternion charges i, j, k. This directly implies that only an even number of nodes are allowed within each gap when considering the whole BZ. Thus, if the Stiefel-Whitney invariant of the flexural band is trivial, then it must also be trivial for the other two bands and there is no protected π_1 charge for this symmetry setting.

Note that this argument holds generally for dynamical matrices, not just in the continuum model, due to the decoupling of the flexural band in the harmonic (noninteracting) approximation discussed in Sec. II A.

V. RELATION TO NAMBU-GOLDSTONE THEOREM

In this section, we discuss more carefully the interplay of the NG theorem and our topological results which we briefly introduced above.

The NG theorem was initially studied for the breaking of internal continuous symmetries in relativistic systems [34,35], where one finds the well-known result that whenever the vacuum of a theory spontaneously breaks a continuous symmetry of the system, massless bosonic excitation (Nambu-Goldstone bosons, NGBs) with linear dispersion appear. The number of NGBs is given by the number of the broken symmetry generator. The generalization of these result to the breaking of space-time symmetries in nonrelativistic theories is discussed in Refs. [36–41]. The main results are that there, in general, are *less* NGBs than the number of broken generators, due to dependencies amongst the generators and that NGBs arising from such dependent generators will generically have a dispersion scaling with an even power of momentum $|\boldsymbol{q}|$. These insights were applied to D-dimensional systems embedded in a d-dimensional space in Ref. [100]. They find the expected number of NGBs only when explicitly taking the lattice structure of the D-dimensional system into account. In particular, they predict two linear and one quadratic band when the symmetry breaking pattern is ISO(3)→ $\mathcal{C}\times$ O(1), where ISO(3) is the group of isometries in 3D, $\mathcal{C}$ is the relevant 2D crystalline group and O(1) = ± 1 corresponds to the out-of-plane $z \rightarrow -z$ symmetry [note that both $\mathcal{C}$ and O(1) are discrete groups]. The symmetry-breaking pattern ISO(3)→ ISO(2)× O(1), on the other hand, corresponding to keeping continuous symmetries in the plane, results in only a single, linear, NGB [100]. Note that this symmetry-breaking pattern is not directly evident in our Lagrangian Eq. (1), as this is only a local expansion around Γ. We now consider what happens if the 2D material is grown on a substrate, which we investigate explicitly for graphene in Sec. VI. Adding a substrate amounts to including a term breaking the O(1) symmetry in the Lagrangian directly. This therefore amounts to an explicit breaking of a discrete symmetry (as opposed to a spontaneous breaking of a continuous symmetry), and we therefore do not expect additional Goldstone modes. Instead, this converts the flexural mode to pseudo-Goldstone bosons, which will, in general, be gapped. Such pseudo-Goldstone modes arise when a symmetry is explicitly broken, as discussed in Refs. [101,102]. This is analogous to a ferromagnetic spin chain: The ground state of a ferromagnetic spin chain violates spin-rotation invariance, resulting in a spontaneously broken symmetry and a single linear NGB (a magnon). However, applying a magnetic field in the z direction amounts to explicitly breaking this symmetry, which gaps the magnon [102]. We therefore expect that growing the material on a substrate should result in the quadratic band (associated with the out-of-plane symmetry) gapping out. This is consistent with our topological analysis, which showed that this band is not protected by a topological invariant and can therefore be gapped from the other bands by small perturbations.

VI. APPLICATION: GRAPHENE

In this section, we apply the above ideas to the paradigmatic 2D material graphene. We show that the nodal charge described in the previous section is nontrivial in this system and that this charge predicts how phonons in graphene will react to the presence of a substrate.

Previous work on phonon topology in free-standing graphene [103,104] have identified various topological nodal points and lines in the spectrum away from Γ. Using methods from topological quantum chemistry (TQC) [8], Ref. [24] studied the symmetry decomposition of the in-plane phonon modes in graphene and found that these modes are globally trivial from the perspective of TQC, though they are close to a fragile phase.

The previous topological analyses do not address the acoustic triple point at Γ. However, we now show that this triple point crossing with the flexural band actually possesses a nontrivial nodal charge (the frame-rotation charge).

There exist a variety of models for graphene, including valence force-field models (VFFMs) [72,76], spring models [103] and symmetry-based tight binding models [105,106]. We implement a VFFM for graphene as described in Ref. [72]. This model explicitly considers six terms: nearest- and next-nearest-neighbor bond stretching, in-plane and out-of plane bending, bond twisting, and interactions with the substrate. The energy associated with each of these terms is written in terms of the displacement of
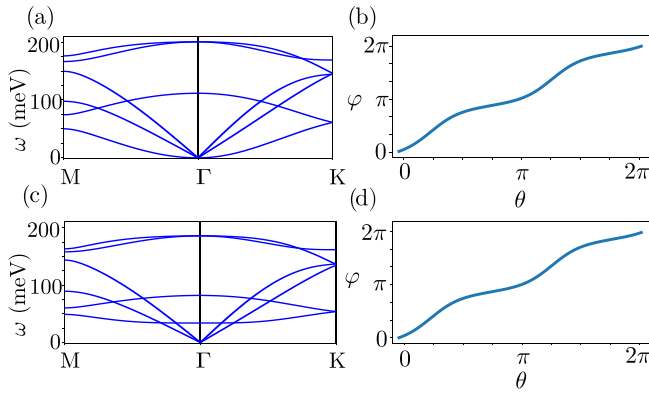
FIG. 3. Phonon band structure and frame rotation charge on a circle around Γ for graphene, based on a valence force-field model from Ref. [72]. (a) Phonon bands along high-symmetry lines for free-standing graphene. (b) Frame rotation charge on a loop around Γ for free-standing graphene. (c), (d) Same as (a) and (b) for graphene on a TaC(111) substrate.

the various atoms in the unit cell, giving a total energy V. In the harmonic approximation, this is differentiated twice with respect to the possible displacements of the atoms in the unit cell. As there are two atoms in the unit cell, which can displaced in three independent directions, this gives a total of six phonon branches. The strength of the various terms in the energy are then treated as fitting parameters to the experimental dispersion, as discussed in Ref. [72]. The term describing interaction with the substrate is zero for free-standing graphene, but nonzero when coupling to a substrate. When this term is nonzero, the acoustic flexural bands gaps out from the other acoustic bands [72,73,96,97].

We consider the case of free-standing graphene as well as graphene on the substrate TaC(111). For both cases, we implement the model described above and solve it on a loop encircling Γ, ensuring that none of the three lower bands touch on the loop and that we are sufficiently close to Γ to avoid any interference from the three upper bands. Before solving, we rotate the dynamical matrix to a real basis. We choose the gauge of the initial point so the matrix $F(\boldsymbol{q})$ in Sec. IV A 1 has determinant $+1$. We can then choose a smooth gauge by choosing the sign of each eigenvector on the loop so it maximizes the overlap with the previous eigenvector. Decomposing the matrix $R(\boldsymbol{q})$ in Sec. IV A 1 into rotation generators, we can then plot the accumulated angle, as shown in Fig. 3, where we also plot the band structure. The model in Ref. [72] is fitted only on the line $\overline{\Gamma M}$, but as we are only interested in a circle around Γ, this suffices for our purposes. Note that there appears to be an additional triple point in the optical phonons at K, but this is an artifact of using a model which is fit only on the line $\overline{\Gamma M}$. In the full first-principle phonon spectrum [107], this triple point is absent. Figures 3(b) and 3(d) show that the nodal charge for free-standing graphene and graphene on TaC(111) is -1. We therefore conclude that this charge is associated with the degeneracy between the linear bands, as the nodal charge does not change when gapping the flexural band. We corroborate these results by repeating the above calculation for free-standing graphene using the symmetry-based model found in Ref. [105], which leads to the same charge.

VII. CONCLUSIONS

We have discussed how physical constraints for phonons interplay with symmetry analysis. We summarized the possible nodal charges of acoustic phonons with a reality condition in up to three dimensions in Table I, and discussed in detail how to compute and analyze these charges in 2D.

We have found that acoustic phonons in 2D have an effective inversion symmetry close to Γ, imposed by physical constraints (see Appendix A). This leads to acoustic phonons generically having a quaternionic charge, which, however, is further modified by the physical constraints to be $\{+1, -1\}$. Additionally, the physics dictates that one of the acoustic bands (the flexural band) is completely decoupled from the other bands in the noninteracting limit, which allowed us to identify the nodal charge as belonging to only two of the bands.

Applying the above machinery to graphene, we showed that acoustic phonons in graphene have a nontrivial nodal charge which has not been previously addressed. Knowing that this charge is associated with only two of the bands explains, from a purely topological perspective, the well-known fact that the flexural band of graphene on a substrate can gap from the other acoustic bands.

These points illustrate that symmetry constraints must in certain cases be augmented by physical constraints for band-structure analysis. We anticipate that similar effects could arise in other physical contexts. One example may be photonic lattices. In this context, optical responses necessarily feature a Bosonic spectrum with an inherent particle-hole symmetry, as well as persistent zero modes that are rather similar to an acoustic mode. This can also lead to triple nodes at zero frequency that are not rooted in symmetry (in fact, irreducible representations cannot formally be assigned in this case).

Finally, from a theoretical perspective it could be interesting to relate the above types of analyses to topological charges of nonlinear sigma models. Such sigma models have recently also been evaluated from a Flag manifold perspective, as in this paper (see, e.g., Ref [108]). It would therefore be interesting to investigate whether these mathematical results find solid ground in the context we have considered.

APPENDIX A: FURTHER CONSTRAINTS ON THE DYNAMICAL MATRIX

In this section, we analyze the restrictions on the dynamical matrix around Γ ($\boldsymbol{q} = \boldsymbol{0}$), which arise from constraints that are not intrinsically captured by a pure space group analysis. These constraints set the phonon problem apart from

the corresponding electronic problem. We mostly discuss the case with TRS but briefly comment on the magnetic case in Appendix A 2.

1. Constraints with time-reversal symmetry

Let us begin by briefly reviewing the constraints that the Bloch Hamiltonian $H(\boldsymbol{k})$ of a nonmagnetic electronic system on a lattice should satisfy. The only required symmetry operations in this setting are lattice translations and time reversal. Working perturbatively close to Γ, we can work with an effective continuum (local) model $\tilde{H}(\boldsymbol{k})$. The only constraints on permissible local Hamiltonians are then unitarity, i.e., $H(\boldsymbol{k}) = H^\dagger(\boldsymbol{k})$ and TRS, i.e., $UH^*(-\boldsymbol{k})U^\dagger = H(\boldsymbol{k})$ for some unitary operator U. Depending on whether spin-orbit coupling can be discarded or not, the TRS operator may square to $+1$ (-1), corresponding, respectively, to AZ class AI or AII. Additional constraints on the Bloch Hamiltonian may arise from spatial symmetries. Such constraints have been extensively analyzed in the literature [1,7–10,62] and form the symmetry classification of the Bloch Hamiltonian, based on an analysis of space groups.

We now turn to describing phononic systems and show that the same constraints emerge but that they are supplemented by additional conditions due to the physical constraints discussed in Sec. I. We consider the dynamical matrix in the harmonic approximation which, in any dimension, is given by [109,110]

$$D_{\alpha\beta}(ss'|\boldsymbol{q}) = \frac{1}{\sqrt{m_s m'_s}} \sum_{\vec{l}} \Phi_{\alpha\beta}(\vec{0}s; \vec{l}s') e^{i\boldsymbol{q}\cdot\boldsymbol{x}(\vec{l})}, \quad \text{(A1)}$$

where α, β label the Cartesian coordinates; s, s' label the atoms in the unit cell with masses $m_s, m_{s'}$; $\vec{l}$ enumerates the unit cells with coordinate $\boldsymbol{x}(\vec{l})$ and $\Phi_{\alpha\beta}(\vec{0}s; \vec{l}s')$ is the force constant matrix in the harmonic approximation:

$$\Phi_{\alpha\beta}(\vec{l}s; \vec{l}'s') = \left.\frac{\partial^2 V}{\partial u_\alpha(\vec{l}s)\partial u_\beta(\vec{l}'s')}\right|_{u=0}. \quad \text{(A2)}$$

Here V is the total potential energy, $u_\alpha(\vec{l}s)$ is the displacement along α of atom s in unit cell $\vec{l}$, and the matrix is evaluated at the equilibrium position of the atoms. Because we expect that Φ is real, we immediately find

$$D_{\alpha\beta}(ss'|\boldsymbol{q}) = D_{\alpha\beta}^*(ss'|-\boldsymbol{q}). \quad \text{(A3)}$$

Thus, we automatically satisfy spinless TRS in this formalism. (We provide a brief overview of how to break TRS in phononic systems in Appendix A 2. A more detailed discussion can be found in Ref. [33].) Furthermore, by commuting the partial derivatives, we find

$$\Phi_{\alpha\beta}(\vec{l}s, \vec{l}'s') = \Phi_{\beta\alpha}(\vec{l}'s'; \vec{l}s), \quad \text{(A4)}$$

which implies that $D_{\alpha\beta}(ss'|\boldsymbol{q}) = D_{\beta\alpha}(s's|\boldsymbol{q})$. As shown in Ref. [110], it follows that D is Hermitian. We note that it is *not* generally true that $D(\boldsymbol{q}) = UD(-\boldsymbol{q})U^\dagger$ for some unitary U (this condition is what we refer to in the main text as generalized inversion symmetry). Therefore, $D(\boldsymbol{q})$ is not, in general, unitarily equivalent to a real matrix.

So far, all results are analogous to the nonmagnetic electronic case and, just like the electronic case, additional constraints can now arise from crystalline symmetries. However, even without additional symmetries, there are further constraints (for stable structures) on the form of $D(\boldsymbol{q})$ which are not present for the Bloch Hamiltonian $H(\boldsymbol{k})$. As discussed in Sec. I, $D(\boldsymbol{q})$ must be positive semidefinite to avoid imaginary frequencies, which correspond to an unstable structure. Furthermore, there should be an appropriate number of zero-energy acoustic bands at $\boldsymbol{q} = \boldsymbol{0}$, as dictated by the NG theorem. We here assume that the NG theorem is not modified by any substrate. It turns out that these constraints are sufficient to guarantee that the nodal charge of the *acoustic* bands at Γ is always captured by real topology.

To show this, let us focus on some region around Γ in the BZ. Sufficiently close to Γ, we can construct an effective dynamical matrix $\tilde{D}(\boldsymbol{q})$ containing *only* the acoustic bands, e.g., if there are N acoustic bands then $\tilde{D}(\boldsymbol{q})$ is an $N \times N$ matrix. This is guaranteed from the fact that the acoustic modes all go to zero, allowing the decoupling from the optical modes [111]. We require that all eigenvalues of $\tilde{D}(\boldsymbol{0})$ are zero, so $\tilde{D}(\boldsymbol{0}) = \mathbb{0}$. As this is an effective model, we do not require it to be positive semidefinite everywhere. Instead, we only require that it should be positive semidefinite on a ball B_ϵ of radius ϵ in $\boldsymbol{q}$ space surrounding Γ, where we also assume that the acoustic bands stay detached from all optical bands on B_ϵ. We assume throughout that $\epsilon > 0$. We can now expand $\tilde{D}(\boldsymbol{q})$ in powers of $\boldsymbol{q}$ in B_ϵ, where we note that the condition $\tilde{D}(\boldsymbol{q}) = \mathbb{0}$ precludes a constant term. We denote the (fixed) basis matrices for $N \times N$ Hermitian matrices by $\{\Gamma_i\}_{i=1}^{N^2}$ (these can be chosen to be the identity and the Pauli matrices for $N = 2$ and the identity and the Gell-Mann matrices for $N = 3$). The most general form of the dynamical matrix is then

$$\tilde{D}(\boldsymbol{q}) = \alpha_1^{jk} q_j \Gamma_k + \alpha_2^{lmn} q_l q_m \Gamma_n + O(\boldsymbol{q}^3), \quad \text{(A5)}$$

where the summation convention for repeated indices has been assumed. Positive semidefiniteness requires that

$$z\tilde{D}(\boldsymbol{q})z^* \geqslant 0 \quad \forall z \in \mathbb{C}^N. \quad \text{(A6)}$$

Let us now assume that the lowest order term that appears in the expansion is of order k, and assume that $\tilde{D}(\boldsymbol{q})$ is positive definite for $\boldsymbol{q} \in B_\epsilon$. Then, sufficiently close to Γ,

$$\alpha_k^{i_1...i_k n} q_{i_1} \ldots q_{i_k} z \Gamma_n z^* \geqslant 0 \quad \forall z \in \mathbb{C}^N. \quad \text{(A7)}$$

Fixing a $z \in \mathbb{C}^N \backslash \{0\}$, the same equation must hold at $-\boldsymbol{q}$, which by assumption is also in B_ϵ. This clearly requires that k be even, which gives the kth order term an effective $\mathcal{PT}$ symmetry. Sufficiently close to Γ, only the term of order k will matter. Therefore, there will always be an effective $\mathcal{PT}$ symmetry sufficiently close to Γ.

We note finally that the positive semidefinite condition does not further constrain the number of permissible matrices $\{\Gamma_i\}$ that can appear in $\tilde{D}(\boldsymbol{q})$ as it is always possible to choose a basis for Hermitian matrices consisting exclusively of positive semidefinite matrices. TRS will, in general, constrain the number of basis matrices, but this feature is shared between the phononic and the electronic case.

2. Breaking time-reversal symmetry in phononic systems

Phonons, as opposed to electrons, are electrically neutral. We therefore, *a priori*, do not expect them to couple strongly to an external magnetic field, and therefore breaking of TRS is a much more exotic effect in phonons than it is in electrons. There are, however, various proposals to break TRS. Some ideas include Raman spin-phonon couplings [44,112], pseudomagnetic fields induced by the Coriolis force [48,49,58], and optomechanical interactions [52]. This clearly goes beyond the standard formulation of the dynamical matrix discussed in the previous section, which automatically incorporates TRS [see Eq. (A3)].

The way around this is to introduce extra terms in the Lagrangian. A summary of these effects can be found in Ref. [33]. However, for noninteracting phononic band structures in the 80 layer groups in AZ class AI, such effects do not occur. We therefore do not discuss the breaking of TRS further in this paper.

APPENDIX B: ACOUSTIC PHONONS IN 3D AND 1D

1. Acoustic phonons in 3D

The continuum model for acoustic phonons in 3D can be derived in a similar fashion as the 2D model [75]. There are no flexural modes and in the continuum model, two of the linearly dispersing bands are degenerate. Concretely, the dynamical matrix (with $\boldsymbol{q} = [q_x, q_y, q_z]$) is

$$D(\boldsymbol{q}) = \begin{pmatrix} v_{3,T}^2 \boldsymbol{q}^2 & (v_{3,L}^2 - v_{3,T}^2)q_x q_y & (v_{3,L}^2 - v_{3,T}^2)q_x q_z \\ (v_{3,L}^2 - v_{3,T}^2)q_x q_y & v_{3,T}^2 \boldsymbol{q}^2 & (v_{3,L}^2 - v_{3,T}^2)q_y q_z \\ (v_{3,L}^2 - v_{3,T}^2)q_x q_z & (v_{3,L}^2 - v_{3,T}^2)q_y q_z & v_{3,T}^2 \boldsymbol{q}^2 \end{pmatrix}, \tag{B1}$$

where $v_{3,T}$ and $v_{3,L}$ are the transverse and longitudinal velocities in 3D, respectively. In terms of elastic parameters, these are given by $v_l = \sqrt{(\lambda + 2\mu)/\rho_0}$ and $v_t = \sqrt{\mu/\rho_0}$. The explicit eigenfrequencies of this model are given by

$$\omega_1^2 = v_{3,L}^2 \boldsymbol{q}^2, \tag{B2}$$

$$\omega_2^2 = v_{3,T}^2 \boldsymbol{q}^2, \tag{B3}$$

$$\omega_3^2 = v_{3,T}^2 \boldsymbol{q}^2. \tag{B4}$$

The topology of this model was considered in Ref. [74]. In agreement with Table I, they find that it is characterized by a Euler charge over a closed surface, as long as there is a gap between ω_2 and ω_3 away from Γ. Adding symmetry constraints can force the three bands to cross along high-symmetry lines emanating from Γ, which prevents the definition of a topological charge. As discussed in Ref. [74], this happens when v_L and v_T become $\boldsymbol{q}$ dependent and change relative magnitude along high-symmetry lines. By building more complicated models, it may also be possible to lift the two-band degeneracy away from Γ, allowing a multigap partitioning not discussed in Ref. [74]. However, as can be seen in Table I, such a multigap system would have trivial charge.

even if the strain tensor $\overset{\leftrightarrow}{u}_{ij}$ is small. This is the case for torsional modes, which correspond to a twisting of the 1D material. Torsional acoustic modes have a linear dispersion relation [75]. Such modes have frequently been studied in carbon nanotubes [113–115], but have also been seen in other materials [116]. Thus, in rod geometries, we expect two linear and two quadratic modes, where the quadratic modes are degenerate if the system has radial symmetry. There may also be other symmetries which make the two linear bands degenerate. We note further that we still expect the arguments in Appendix A to hold, so the dynamical matrix can be chosen to be (locally) real. The relevant homotopy groups (see Sec. III) are then $\pi_0(M)$, where the classifying space M can be $\mathrm{Fl}_{1,1,1,1}^{\mathbb{R}} = \mathrm{SO}(4)/\mathrm{S}[\mathrm{O}(1) \times \mathrm{O}(1) \times \mathrm{O}(1) \times \mathrm{O}(1)]$, corresponding to a $1 \oplus 1 \oplus 1 \oplus 1$ split, or the partial Flag variety $\mathrm{Fl}_{2,1,1}^{\mathbb{R}} = \mathrm{SO}(4)/\mathrm{S}[\mathrm{O}(1) \times \mathrm{O}(1) \times \mathrm{O}(2)]$ corresponding to a $2 \oplus 1 \oplus 1$ split (equivalent to a $1 \oplus 1 \oplus 2$ split) or $\mathrm{Gr}_{2,4}^{\mathbb{R}} = \mathrm{SO}(4)/\mathrm{S}[\mathrm{O}(2) \times \mathrm{O}(2)]$, corresponding to a $2 \oplus 2$ split. However, the homotopy charge $\pi_0(M)$ is trivial for all of these classifying spaces, so it does not seem possible to stabilize this fourfold crossing by using a topological argument. We leave the investigation of the stability of such a fourfold crossing to future work.

APPENDIX C: NON-ABELIAN WILSON LOOPS AND THE LIFTING MAP

1. The lifting map

For completeness, we also include a method for distinguishing all five conjugacy classes of the quaternion group $\mathbb{Q}$, $\{1, -1, \pm i, \pm j, \pm k\}$ without having to split the nodes as done in Sec. IV A 2. This method was introduced in Ref. [70]. The idea is to lift the SO(3) valued Wilson loop to an SU(2) valued version, being isomorphic to the quaternions with unit norm. We start with the SO(3) valued Berry connection which

2. Acoustic phonons in 1D

To study 1D materials, we choose a rod geometry where the material is extended in the z direction, with a very small radius in the xy plane. There are then two flexural modes, with velocities $v_{h,x}, v_{h,y}$ dependent on the moment of mass in the x and y directions, respectively [75]. If the material has radial symmetry around the z axis (the extended axis), then $v_{h,x} = v_{h,y}$, and we get a doubly degenerate flexural mode with quadratic dispersion. There is, however, one subtlety in the 1D case: the displacement field $\boldsymbol{u}(z)$ can be large

in component reads

$$[A(\boldsymbol{q})_a]_j^i = \langle u_{\boldsymbol{q}}^i | \partial_{\boldsymbol{q}_a} | u_{\boldsymbol{q}}^j \rangle, \tag{C1}$$

with $a \in \{x, y\}$ and $i, j \in \{1, 2, 3\}$. Being SO(3) valued, $A(\boldsymbol{q})$ can be decomposed into the basis matrices of the Lie algebra $\{L_i\}_{i=x,y,z}$. These can then be lifted to the Lie algebra of the double cover SU(2) by replacing $\{L_i\}_{i=x,y,z}$ with the corresponding Dirac matrices, which in this case equals $-\frac{i}{2}\sigma_{x,y,z}$. This gives the lifted connection $\tilde{A}(\boldsymbol{q})$ which is SU(2) valued. Then, computing the standard Wilson loop,

$$n_\Delta = \overline{\exp}\left(\oint_\Delta \tilde{A}(\boldsymbol{q}) \cdot d\boldsymbol{q}\right), \tag{C2}$$

along a contour Δ, gives $n_\Delta \in$ SU(2), which is isomorphic to the quaternionic group $\mathbb{Q}$ with unit norm. We remark that care must be taken when computing the exponential, as the different matrices in the exponent do not generically commute.

For the simple model in Eq. (4), this quantity is easily computed and we show in the next section that we get $n_\Delta = -\mathbb{1}$, in agreement with what was found by the other computations in Sec. IV. For more complicated systems, an approximation of this expression, using the Baker-Campbell-Hausdorff formula, is given in Ref. [70]. We numerically compute this quantity for the graphene system considered in Sec. VI and find that it always agrees with our observed frame rotation charge when only considering the lower three bands. However, considering all six bands [e.g., lifting SO(6) to spin(6)$\simeq$ SU(4)] gives a trivial charge, which shows that the three optical bands also carry a nontrivial frame rotation charge. This originates from the degeneracy of the optical bands at Γ, visible in Fig. 3.

2. Computing n_Δ for the continuum model

In this section, we compute the non-Abelian Wilson loop charge n_Δ explicitly for the simple model in Eq. (4). Once again, ordering by frequency, we get

$$A_x = \langle u_i | \partial_{q_x} | u_j \rangle = \frac{1}{|\boldsymbol{q}|^2}\begin{pmatrix} 0 & 0 & 0 \\ 0 & 0 & -q_y \\ 0 & q_y & 0 \end{pmatrix} = \frac{q_y}{|\boldsymbol{q}|^2}L_x,$$

$$A_y = \langle u_i | \partial_{q_y} | u_j \rangle = \frac{1}{|\boldsymbol{q}|^2}\begin{pmatrix} 0 & 0 & 0 \\ 0 & 0 & q_x \\ 0 & -q_x & 0 \end{pmatrix} = -\frac{q_x}{|\boldsymbol{q}|^2}L_x.$$

We note that this agrees with our observation from Sec. IV A 1 that, because one band is decoupled, the eigenvectors are rotated around a fixed axis. We perform the lift by replacing $L_x \to -\frac{i}{2}\sigma_x$. Then, letting $\boldsymbol{q}$ be along a loop away from the origin gives

$$\tilde{A}(\boldsymbol{q}) \cdot d\boldsymbol{q} = \frac{i}{2}\sigma_x d\theta. \tag{C3}$$

This is independent of $\boldsymbol{q}$, so every matrix in the exponential commutes. Letting Δ be a circle in the BZ, we then find

$$n_\Delta = \overline{\exp}\left(\oint_\Delta \tilde{A}(\boldsymbol{q}) \cdot d\boldsymbol{q}\right) = \exp(i\pi\sigma_x) = -\mathbb{1}, \tag{C4}$$

in agreement with what we found in Sec. IV.

[1] L. Fu, Topological Crystalline Insulators, Phys. Rev. Lett. **106**, 106802 (2011).

[2] K. Shiozaki and M. Sato, Topology of crystalline insulators and superconductors, Phys. Rev. B **90**, 165114 (2014).

[3] J. Höller and A. Alexandradinata, Topological Bloch oscillations, Phys. Rev. B **98**, 024310 (2018).

[4] V. Juričić, A. Mesaros, R.-J. Slager, and J. Zaanen, Universal Probes of Two-Dimensional Topological Insulators: Dislocation and π Flux, Phys. Rev. Lett. **108**, 106403 (2012).

[5] C.-K. Chiu, J. C. Y. Teo, A. P. Schnyder, and S. Ryu, Classification of topological quantum matter with symmetries, Rev. Mod. Phys. **88**, 035005 (2016).

[6] Z. Song, T. Zhang, Z. Fang, and C. Fang, Quantitative mappings between symmetry and topology in solids, Nat. Commun. **9**, 3530 (2018).

[7] H. C. Po, A. Vishwanath, and H. Watanabe, Symmetry-based indicators of band topology in the 230 space groups, Nat. Commun. **8**, 50 (2017).

[8] B. Bradlyn, L. Elcoro, J. Cano, M. G. Vergniory, Z. Wang, C. Felser, M. I. Aroyo, and B. A. Bernevig, Topological quantum chemistry, Nature (London) **547**, 298 (2017).

[9] R.-J. Slager, A. Mesaros, V. Juričić, and J. Zaanen, The space group classification of topological band-insulators, Nat. Phys. **9**, 98 (2013).

[10] J. Kruthoff, J. de Boer, J. van Wezel, C. L. Kane, and R.-J. Slager, Topological Classification of Crystalline Insulators Through Band Structure Combinatorics, Phys. Rev. X **7**, 041069 (2017).

[11] A. Bouhon, T. Bzdušek, and R.-J. Slager, Geometric approach to fragile topology beyond symmetry indicators, Phys. Rev. B **102**, 115135 (2020).

[12] A. Bouhon, G. F. Lange, and R.-J. Slager, Topological correspondence between magnetic space group representations and subdimensions, Phys. Rev. B **103**, 245127 (2021).

[13] H. Watanabe, H. C. Po, and A. Vishwanath, Structure and topology of band structures in the 1651 magnetic space groups, Sci. Adv. **4**, eaat8685 (2018).

[14] R.-J. Slager, The translational side of topological band insulators, J. Phys. Chem. Solids **128**, 24 (2019).

[15] L. Elcoro, B. J. Wieder, Z. Song, Y. Xu, B. Bradlyn, and B. A. Bernevig, Magnetic topological quantum chemistry, Nat. Commun. **12**, 5965 (2021).

[16] H. C. Po, H. Watanabe, and A. Vishwanath, Fragile Topology and Wannier Obstructions, Phys. Rev. Lett. **121**, 126402 (2018).

[17] G. F. Lange, A. Bouhon, and R.-J. Slager, Subdimensional topologies, indicators, and higher order boundary effects, Phys. Rev. B **103**, 195145 (2021).

[18] D. S. Borgnia, A. J. Kruchkov, and R.-J. Slager, Non-hermitian Boundary Modes and Topology, Phys. Rev. Lett. **124**, 056802 (2020).

[19] J.-W. Rhim, J. H. Bardarson, and R.-J. Slager, Unified bulk-boundary correspondence for band insulators, Phys. Rev. B **97**, 115143 (2018).

[20] Z.-D. Song, L. Elcoro, Y.-F. Xu, N. Regnault, and B. A. Bernevig, Fragile Phases as Affine Monoids: Classification and Material Examples, Phys. Rev. X **10**, 031001 (2020).

[21] R.-J. Slager, A. Mesaros, V. Juričić, and J. Zaanen, Interplay between electronic topology and crystal symmetry: Dislocation-line modes in topological band insulators, Phys. Rev. B **90**, 241403(R) (2014).

[22] V. Peri, Z.-D. Song, M. Serra-Garcia, P. Engeler, R. Queiroz, X. Huang, W. Deng, Z. Liu, B. A. Bernevig, and S. D. Huber, Experimental characterization of fragile topology in an acoustic metamaterial, Science **367**, 797 (2020).

[23] S. S. Mathias and R.-J. Slager, Unsupervised machine learning and band topology, Phys. Rev. Lett. **124**, 226401 (2020).

[24] J. L. Mañes, Fragile phonon topology on the honeycomb lattice with time-reversal symmetry, Phys. Rev. B **102**, 024307 (2020).

[25] B. Peng, Y. Hu, S. Murakami, T. Zhang, and B. Monserrat, Topological phonons in oxide perovskites controlled by light, Sci. Adv. **6**, eabd1618 (2020).

[26] D. S. Tang and B. Y. Cao, Topological effects of phonons in GaN and AlGaN: A potential perspective for tuning phonon transport, J. Appl. Phys. **129**, 085102 (2021).

[27] J. Li, J. Liu, S. A. Baronett, M. Liu, L. Wang, R. Li, Y. Chen, D. Li, Q. Zhu, and X. Q. Chen, Computation and data driven discovery of topological phononic materials, Nat. Commun. **12**, 1204 (2021).

[28] A. Altland and M. R. Zirnbauer, Nonstandard symmetry classes in mesoscopic normal-superconducting hybrid structures, Phys. Rev. B **55**, 1142 (1997).

[29] A. P. Schnyder, S. Ryu, A. Furusaki, and A. W. W. Ludwig, Classification of topological insulators and superconductors in three spatial dimensions, Phys. Rev. B **78**, 195125 (2008).

[30] A. Kitaev, Periodic table for topological insulators and superconductors, AIP Conf. Proc. **1134**, 22 (2009).

[31] C. L. Kane and T. C. Lubensky, Topological boundary modes in isostatic lattices, Nat. Phys. **10**, 39 (2014).

[32] H. C. Po, Y. Bahri, and A. Vishwanath, Phonon analog of topological nodal semimetals, Phys. Rev. B **93**, 205158 (2016).

[33] Y. Liu, X. Chen, and Y. Xu, Topological phononics: From fundamental models to real materials, Adv. Funct. Mater. **30**, 1904784 (2020).

[34] Y. Nambu, Quasi-particles and gauge invariance in the theory of superconductivity, Phys. Rev. **117**, 648 (1960).

[35] J. Goldstone, Field theories with "superconductor" solutions, Nuovo Cim **19**, 154 (1961).

[36] H. B. Nielsen and S. Chadha, On how to count Goldstone bosons, Nucl. Phys. B **105**, 445 (1976).

[37] H. Watanabe and T. Brauner, Number of Nambu-gGoldstone bosons and its relation to charge densities, Phys. Rev. D **84**, 125013 (2011).

[38] H. Watanabe and H. Murayama, Redundancies in Nambu-Goldstone Bosons, Phys. Rev. Lett. **110**, 181601 (2013).

[39] Y. Hidaka, Counting Rule for Nambu-Goldstone Modes in Nonrelativistic Systems, Phys. Rev. Lett. **110**, 091601 (2013).

[40] I. Arraut, The Nambu-Goldstone theorem in nonrelativistic systems, Int. J. Mod. Phys. A **32**, 1750127 (2017).

[41] H. Watanabe, Counting rules of Nambu-Goldstone modes, Annu. Rev. Condens. Matter Phys. **11**, 169 (2020).

[42] D. V. Else, Topological Goldstone phases of matter, Phys. Rev. B **104**, 115129 (2021).

[43] E. Prodan and C. Prodan, Topological Phonon Modes and Their Role in Dynamic Instability of Microtubules, Phys. Rev. Lett. **103**, 248101 (2009).

[44] L. Zhang, J. Ren, J. S. Wang, and B. Li, Topological Nature of the Phonon Hall Effect, Phys. Rev. Lett. **105**, 225901 (2010).

[45] N. Li, J. Ren, L. Wang, G. Zhang, P. Hänggi, and B. Li, Colloquium: Phononics: Manipulating heat flow with electronic analogs and beyond, Rev. Mod. Phys. **84**, 1045 (2012).

[46] M. Maldovan, Sound and heat revolutions in phononics, Nature (London) **503**, 209 (2013).

[47] S. Roman and D. H. Sebastian, Observation of phononic helical edge states in a mechanical topological insulator, Science **349**, 47 (2015).

[48] P. Wang, L. Lu, and K. Bertoldi, Topological Phononic Crystals with One-Way Elastic Edge Waves, Phys. Rev. Lett. **115**, 104302 (2015).

[49] Y. T. Wang, P. G. Luan, and S. Zhang, Coriolis force induced topological order for classical mechanical vibrations, New J. Phys. **17**, 073031 (2015).

[50] Z. Yang, F. Gao, X. Shi, X. Lin, Z. Gao, Y. Chong, and B. Zhang, Topological Acoustics, Phys. Rev. Lett. **114**, 114301 (2015).

[51] L. M. Nash, D. Kleckner, A. Read, V. Vitelli, A. M. Turner, and W. T. M. Irvine, Topological mechanics of gyroscopic metamaterials, Proc. Natl. Acad. Sci. USA. **112**, 14495 (2015).

[52] V. Peano, C. Brendel, M. Schmidt, and F. Marquardt, Topological Phases of Sound and Light, Phys. Rev. X **5**, 031011 (2015).

[53] S. D. Huber, Topological mechanics, Nat. Phys. **12**, 621 (2016).

[54] R. Süsstrunk and S. D. Huber, Classification of topological phonons in linear mechanical metamaterials, Proc. Natl. Acad. Sci. USA **113**, E4767 (2016).

[55] T. Kariyado and R.-J. Slager, π-fluxes, semimetals, and flat bands in artificial materials, Phys. Rev. Res. **1**, 032027(R) (2019).

[56] T. Kariyado and R.-J. Slager, Selective branching and converting of topological modes, Phys. Rev. Res. **3**, L032035 (2021).

[57] Y. Liu, Y. Xu, S. C. Zhang, and W. Duan, Model for topological phononics and phonon diode, Phys. Rev. B **96**, 064106 (2017).

[58] M. Di Liberto, A. Kruckenhauser, P. Zoller, and M. A. Baranov, Topological phonons in arrays of ultracold dipolar particles, arXiv:2108.11856.

[59] S. Shankar, P. Bryde, and L. Mahadevan, Geometric control of topological dynamics in a singing saw, arXiv:2108.10875.

[60] R.-J. Slager, V. Juričić, V. Lahtinen, and J. Zaanen, Self-organized pseudo-graphene on grain boundaries in topological band insulators, Phys. Rev. B **93**, 245406 (2016).

[61] V. Kopský (Editor) and D. B. Litvin (Editor), *International Tables for Crystallography* Volume E, 2nd Edition, Subperiodic Groups (Wiley, Hoboken, NJ, 2010).

[62] C. J. Bradley and A. P. Cracknell, *The Mathematical Theory of Symmetry in Solids* (Oxford University Press, Oxford, 1972).

[63] M. I. Aroyo, A. Kirov, C. Capillas, J. M. Perez-Mato, and H. Wondratschek, Bilbao Crystallographic Server. II.

Representations of crystallographic point groups and space groups, Acta Crystallogr. Sec. A **62**, 115 (2006).

[64] V. Könye, A. Bouhon, I. C. Fulga, R.-J. Slager, J. van den Brink, and J. I. Facio, Chirality flip of Weyl nodes and its manifestation in strained $MoTe_2$, Phys. Rev. Res. **3**, L042017 (2021).

[65] A. Bouhon, Q. Wu, R.-J. Slager, H. Weng, O. V. Yazyev, and T. Bzdušek, Non-Abelian reciprocal braiding of Weyl points and its manifestation in ZrTe, Nat. Phys. **16**, 1137 (2020).

[66] S. Chen, A. Bouhon, R.-J. Slager, and B. Monserrat, Manipulation and braiding of Weyl nodes using symmetry-constrained phase transitions, arXiv:2108.10330.

[67] A. Tiwari and T. Bzdušek, Non-Abelian topology of nodal-line rings in PT-symmetric systems, Phys. Rev. B **101**, 195130 (2020).

[68] T. Bzdušek and M. Sigrist, Robust doubly charged nodal lines and nodal surfaces in centrosymmetric systems, Phys. Rev. B **96**, 155105 (2017).

[69] A. Bouhon, A. M. Black-Schaffer, and R.-J. Slager, Wilson loop approach to fragile topology of split elementary band representations and topological crystalline insulators with time-reversal symmetry, Phys. Rev. B **100**, 195135 (2019).

[70] Q. Wu, A. A. Soluyanov, and T. Bzdušek, Non-Abelian band topology in noninteracting metals, Science **365**, 1273 (2019).

[71] F. N. Ünal, A. Bouhon, and R.-J. Slager, Topological Euler Class as a Dynamical Observable in Optical Lattices, Phys. Rev. Lett. **125**, 053601 (2020).

[72] T. Aizawa, R. Souda, S. Otani, Y. Ishizawa, and C. Oshima, Bond softening in monolayer graphite formed on transition-metal carbide surfaces, Phys. Rev. B **42**, 11469 (1990).

[73] A. Al Taleb and D. Farías, Phonon dynamics of graphene on metals, J. Phys. Condens. Matter **28**, 103005 (2016).

[74] S. Park, Y. Hwang, H. C. Choi, and B. J. Yang, Topological acoustic triple point, Nat. Commun. **12**, 6781 (2021).

[75] L. D. Landau, E. M. Lifshits, A. M. Kosevich, and L. P. Pitaevskii, *Theory of Elasticity* (Butterworth-Heinemann, Oxford, 1986).

[76] J. W. Jiang, B. S. Wang, J. S. Wang, and H. S. Park, A review on the flexural mode of graphene: Lattice dynamics, thermal conduction, thermal expansion, elasticity and nanomechanical resonance, J. Phys.: Condens. Matter **27**, 083001 (2015).

[77] E. Mariani and F. von Oppen, Flexural Phonons in Free-Standing Graphene, Phys. Rev. Lett. **100**, 076801 (2008).

[78] S. Sachdev and D. R. Nelson, Crystalline and fluid order on a random topography, J. Phys. C: Solid State Phys. **17**, 5473 (1984).

[79] A. N. Rudenko, A. V. Lugovskoi, A. Mauri, G. Yu, S. Yuan, and M. I. Katsnelson, Interplay between in-plane and flexural phonons in electronic transport of two-dimensional semiconductors, Phys. Rev. B **100**, 075417 (2019).

[80] A. Taheri, S. Pisana, and C. V. Singh, Importance of quadratic dispersion in acoustic flexural phonons for thermal transport of two-dimensional materials, Phys. Rev. B **103**, 235426 (2021).

[81] M. Nakahara, *Geometry, Topology and Physics* (CRC Press, Boca Raton, 2003).

[82] C. Chicone, Elasticity: Basic theory and equations of motion, in *An Invitation to Applied Mathematics* (Academic Press, Cambridge, MA, 2017), Chap. 18, pp. 577–670.

[83] M. H. Sadd, Material behavior-linear elastic solids, in *Elasticity*, 4th ed., edited by Martin H. Sadd (Academic Press, Oxford, 2021), Chap. 4, pp. 83–96.

[84] A. Hatcher, *Algebraic Topology* (Cambridge University Press, Cambridge, 2001).

[85] J. Ahn, D. Kim, Y. Kim, and B.-J. Yang, Band Topology and Linking Structure of Nodal Line Semimetals with Z_2 Monopole Charges, Phys. Rev. Lett. **121**, 106403 (2018).

[86] C. C. Wojcik, X.-Q. Sun, T. Bzdušek, and S. Fan, Homotopy characterization of non-hermitian Hamiltonians, Phys. Rev. B **101**, 205417 (2020).

[87] J. Ahn, S. Park, D. Kim, Y. Kim, and B.-J. Yang, Stiefel-whitney classes and topological phases in band theory, Chin. Phys. B **28**, 117101 (2019).

[88] J. Ahn, S. Park, and B.-J. Yang, Failure of Nielsen-Ninomiya Theorem and Fragile Topology in Two-Dimensional Systems with Space-Time Inversion Symmetry: Application to Twisted Bilayer Graphene at Magic Angle, Phys. Rev. X **9**, 021013 (2019).

[89] We note that the nontrivial element of $\pi_1[Gr_{3,N \geq 4}^{\mathbb{R}}] = \mathbb{Z}_2$ [68] would correspond to a nodal point with a π-Berry phase connecting the three acoustic bands with higher bands, contrary to the assumption that the acoustic bands are separated from all the other bands in the vicinity of Γ.

[90] B. Jiang, A. Bouhon, Z.-K. Lin, X. Zhou, B. Hou, F. Li, R.-J. Slager, and J.-H. Jiang, Experimental observation of non-Abelian topological acoustic semimetals and their phase transitions, Nat. Phys. **17**, 1239 (2021).

[91] B. Peng, A. Bouhon, B. Monserrat, and R.-J. Slager, Phonons as a platform for non-Abelian braiding and its manifestation in layered silicates, Nat. Commun. **13**, 423 (2022).

[92] B. Peng, A. Bouhon, R.-J. Slager, and B. Monserrat, Multigap topology and non-Abelian braiding of phonons from first principles arXiv:2111.05872.

[93] Q. Guo, T. Jiang, R.-Y. Zhang, L. Zhang, Z.-Q. Zhang, B. Yang, S. Zhang, and C. T. Chan, Experimental observation of non-Abelian topological charges and edge states, Nature (London) **594**, 195 (2021).

[94] A. J. Beekman, J. Nissinen, K. Wu, K. Liu, R.-J. Slager, Z. Nussinov, V. Cvetkovic, and J. Zaanen, Dual gauge field theory of quantum liquid crystals in two dimensions, Phys. Rep. **683**, 1 (2017).

[95] N. Johansson and E. Sjöqvist, Optimal Topological Test for Degeneracies of Real Hamiltonians, Phys. Rev. Lett. **92**, 060406 (2004).

[96] W. L. Z. Zhao, K. S. Tikhonov, and A. M. Finkel'stein, Flexural phonons in supported graphene: From pinning to localization, Sci. Rep. **8**, 16256 (2018).

[97] C. Zhang, L. Cheng, and Y. Liu, Role of flexural phonons in carrier mobility of two-dimensional semiconductors: Free standing vs on substrate, J. Phys.: Condens. Matter **33**, 234003 (2021).

[98] T. Bzdusek, Euler class of a pair of energy bands on a manifold with a boundary, (2020), doi: 10.13140/RG.2.2.29803.69928.

[99] Note that double nodes generically have quadratic band touchings associated with them [90]. However, the eigenvalues of the dynamical matrix $D(\boldsymbol{q})$ correspond to ω^2, so a quadratic eigenmode in $D(\boldsymbol{q})$ corresponds to a linear dispersion as a function of ω.

[100] O. Coquand, Spontaneous symmetry breaking and the flat phase of crystalline membranes, Phys. Rev. B **100**, 125406 (2019).

[101] S. Weinberg, Approximate Symmetries and Pseudo-Goldstone Bosons, Phys. Rev. Lett. **29**, 1698 (1972).

[102] H. Watanabe, T. Brauner, and H. Murayama, Massive Nambu-Goldstone Bosons, Phys. Rev. Lett. **111**, 021601 (2013).

[103] T. Kariyado and Y. Hatsugai, Manipulation of Dirac cones in mechanical graphene, Sci. Rep. **5**, 18107 (2015).

[104] J. Li, L. Wang, J. Liu, R. Li, Z. Zhang, and X.-Q. Chen, Topological phonons in graphene, Phys. Rev. B **101**, 081403(R) (2020).

[105] L. A. Falkovsky, Phonon dispersion in graphene, J. Exp. Theor. Phys. **105**, 397 (2007).

[106] K. H. Michel and B. Verberck, Theory of the evolution of phonon spectra and elastic constants from graphene to graphite, Phys. Rev. B **78**, 085424 (2008).

[107] N. Mounet and N. Marzari, First-principles determination of the structural, vibrational and thermodynamic properties of diamond, graphite, and derivatives, Phys. Rev. B **71**, 205214 (2005).

[108] R. Kobayashi, Y. Lee, K. Shiozaki, and Y. Tanizaki, Topological terms of (2+1)d flag-manifold sigma models, J. High Energy Phys. 08 (2021) 075.

[109] A. A. Maradudin and S. H. Vosko, Symmetry properties of the normal vibrations of a crystal, Rev. Mod. Phys. **40**, 1 (1968).

[110] P. Brüesch, *Phonons: Theory and Experiments I*, Springer Series in Solid-State Sciences (Springer, Berlin, 1982), Vol. 34.

[111] Note that this construction is not guaranteed to work for the substrate case considered in Sec. VI which breaks basal mirror symmetry. Nevertheless, if the lifted flexural band does not cross any of the other acoustic bands close to Γ, then such an effective $\tilde{D}(q)$ still exists for the remaining acoustic bands at Γ.

[112] A. S. Ioselevich and H. Capellmann, Strongly correlated spin-phonon systems: A scenario for heavy fermions, Phys. Rev. B **51**, 11446 (1995).

[113] R. Saito, G. Dresselhaus, and M. S. Dresselhaus, *Physical Properties Of Carbon Nanotubes* (Imperial College Press, London, 1998).

[114] H. M. Lawler, J. W. Mintmire, and C. T. White, Helical strain in carbon nanotubes: Speed of sound and poisson ratio from first principles, Phys. Rev. B **74**, 125415 (2006).

[115] D. Liu, A. G. Every, and D. Tománek, Long-wavelength deformations and vibrational modes in empty and liquid-filled microtubules and nanotubes: A theoretical study, Phys. Rev. B **95**, 205407 (2017).

[116] B. Peng, K. Xu, H. Zhang, Z. Ning, H. Shao, G. Ni, J. Li, Y. Zhu, H. Zhu, and C. M. Soukoulis, 1D SbSeI, SbSI, and SbSBr with high stability and novel properties for microelectronic, optoelectronic, and thermoelectric applications, Adv. Theory Simul. **1**, 1700005 (2018).